

Article

## An Updated Geophysical Model for AMSR-E and SSMIS Brightness Temperature Simulations over Oceans

Elizaveta Zabolotskikh <sup>1,\*</sup>, Leonid Mitnik <sup>2</sup> and Bertrand Chapron <sup>3</sup>

<sup>1</sup> Satellite Oceanography Laboratory, Russian State Hydrometeorological University, Malookhtinsky 98, 195196 St. Petersburg, Russia

<sup>2</sup> V.I. Il'ichev Pacific Oceanological Institute, 43 Baltiyskaya Street, 690041 Vladivostok, Russia; E-Mail: mitnik@poi.dvo.ru

<sup>3</sup> IFREMER, Centre de Brest BP70, 29280 Plouzane, France; E-Mail: bchapron@ifremer.fr

\* Author to whom correspondence should be addressed; E-Mail: lisa@rshu.ru; Tel.: +7-812-372-5085; Fax: +7-812-372-5085.

Received: 10 December 2013; in revised form: 28 February 2014 / Accepted: 4 March 2014 /

Published: 17 March 2014

---

**Abstract:** In this study, we considered the geophysical model for microwave brightness temperature (BT) simulation for the Atmosphere-Ocean System under non-precipitating conditions. The model is presented as a combination of atmospheric absorption and ocean emission models. We validated this model for two satellite instruments—for Advanced Microwave Sounding Radiometer-Earth Observing System (AMSR-E) onboard Aqua satellite and for Special Sensor Microwave Imager/Sounder (SSMIS) onboard F16 satellite of Defense Meteorological Satellite Program (DMSP) series. We compared simulated BT values with satellite BT measurements for different combinations of various water vapor and oxygen absorption models and wind induced ocean emission models. A dataset of clear sky atmospheric and oceanic parameters, collocated in time and space with satellite measurements, was used for the comparison. We found the best model combination, providing the least root mean square error between calculations and measurements. A single combination of models ensured the best results for all considered radiometric channels. We also obtained the adjustments to simulated BT values, as averaged differences between the model simulations and satellite measurements. These adjustments can be used in any research based on modeling data for removing model/calibration inconsistencies. We demonstrated the application of the model by means of the development of the new algorithm for sea surface wind speed retrieval from AMSR-E data.

**Keywords:** satellite passive microwave; AMSR-E; SSMIS; geophysical model; numerical simulation; calibration

---

## 1. Introduction

Satellite passive microwave measurement data remain an invaluable source of regularly available remotely sensed data for environmental studies because they can be quantitatively inverted into the whole set of geophysical parameters independent of time of day and cloud coverage. Low spatial resolution of these data turns into an advantage for operational weather forecast and climatic studies with no artificial smoothing needed. In the polar regions, these data have special value since most radiometers work on polar orbiting satellites, providing the highest time resolution in remote oceanic areas lacking *in situ* measurements. Long-term records of satellite passive microwave radiometer measurements play an important role in climate change monitoring as well as in providing indispensable information for understanding the Earth's climate system, including water and energy circulation. Microwave radiances provided by polar orbiting satellite sensors have become an increasingly important component of observing systems for both global and regional data assimilation systems for numerical weather prediction systems [1,2].

So, undoubted advantages of passive microwave data go side-by-side with the necessity to be strictly consistent in their interpretation, especially for long-term climate studies based on using data from different instruments [3,4]. Such consistency can be ensured both by sensor intercalibration work [5–7] and model calibration studies. The last are based on radiative transfer calculations fulfilled for *in situ* matchup data collocated in time and space with the satellite measurements [8,9]. The quality of the used matchup dataset in any model calibration work acquires not less importance than the quality of the geophysical model used for brightness temperature calculations.

In this study, the simulation of brightness temperatures (BTs) over open oceans under non-precipitating conditions is presented for two satellite passive microwave instruments—for Advanced Microwave Sounding Radiometer-Earth Observing System (AMSR-E) onboard NASA Aqua satellite and for Special Sensor Microwave Imager/Sounder (SSMIS) onboard Defense Meteorological Satellite Program (DMSP) satellites. The geophysical model is comprised of empirical ocean emissivity model and simplified atmospheric absorption model. The atmospheric absorption model takes into account emission and absorption of oxygen, water vapor and cloud liquid water. The applicability of such an approach for the microwave range of frequencies from 5 to 100 GHz, in which AMSR-E and SSMIS channels work, is repeatedly confirmed and proved by many scientific studies [10,11]. As a rule, general differences between various geophysical models concern either the way in which sea surface wind dependency of the ocean emission is taken into account or which of the several water vapor absorption model is used for the atmospheric radiance calculation [2,12]. For low microwave frequency range (L-band) adequate sea water permittivity model becomes also important for the accurate ocean radiance modeling [9,13]. Restriction of the model by non-precipitating conditions is valid for the frequencies less than 37 GHz for clear and cloudy atmosphere and for light rain up to ~2 mm/h [14]. Such a restriction allows using absorption-emission approximation and

neglecting microwave radiation scattering on large rain drops and ice particles. It is estimated [15,16] that only 3% of all global ocean observations relate to the rainfalls with rate more than 2 mm/h. So, non-scattering model is applicable to about 97% of all ocean observations. The imposed absence of rain with large rain rates restricts usage of such geophysical models for the scanning channels up to 37 GHz. For SSMIS sounding channels, influence of rain may be essential only at  $\nu = 50\text{--}53$  GHz. At higher frequencies within the oxygen absorption band the contribution of the ocean and the lower troposphere to the upwelling radiation is small due to high oxygen absorption. Including into consideration higher frequency scanning channels at 85.5 GHz for SSMIS and at 89.0 GHz for AMSR-E requires special care since scattering is observed even for large cloud droplets with diameter  $d > 50\text{--}60$   $\mu\text{m}$  [17].

Obtaining precise geophysical products from satellite passive microwave radiances requires the capability to model the observed radiances with very small systematic and random errors. Systematic errors in calculating microwave brightness temperatures are due to several error sources, first of all due to inadequacies in the radiative transfer models (RTM) [18]. The proposed research aims mainly at the choice of the combination of the atmospheric absorption model and ocean emission model, ensuring the best reproduction of AMSR-E and SSMIS measured brightness temperatures and providing the adjustments to simulated BT values. These adjustments should account integrally both for geophysical model uncertainties and instrument calibration errors. Addition of such adjustments enables the following usage of simulated BTs for geophysical parameter retrieval algorithm development and consistency in estimated parameter series independently on the type of instrument used [19]. Such an approach is particularly important meaning the loss of AMSR-E in October 2011 and the calibration/validation work relating to AMSR2.

It should be emphasized that the obtained adjustments are not claimed to work properly over areas other than open oceans. The correction schemes for the whole range of brightness temperatures need a non-linear and much more complicated approach [20]. However, these adjustments can successfully be used for the atmosphere-open ocean system under proper atmospheric conditions depending on the channel frequency. For example, for AMSR-E low frequency channels at 10.65 and especially at 6.9 GHz even rain does not impede the usage of suggested geophysical model and obtained brightness temperature adjustments.

The described study is comprised of the following consecutive steps. The first step is the atmospheric absorption and ocean emission model simulation, based on the scientific findings of the last years. The second step is the creation of the data set of simultaneous clear sky atmospheric and oceanic parameter measurements and collocated AMSR-E and SSMIS measurements, followed by the comparison of calculated brightness temperatures with measured ones. Such a comparison allows selecting the combination of the models, providing the least averaged differences. The derived averaged differences can be used as corrections to simulated radiances. These corrections can be considered as a final goal of the presented study along with the specified geophysical model. An accurate specification of the geophysical model is the crucial step in developing the geophysical parameter retrieval algorithms. The algorithm development, based on simulated brightness temperatures, can be successfully performed using the selected geophysical model and brightness temperature corrections for handling model/calibration inconsistencies. In this way, we developed a new Neural Network algorithm for sea surface wind speed retrievals from AMSR-E data, using the

same approach as described in [21] and suggested geophysical model. The new geophysical model resulted in new possibilities associated with the adequate performance of the new algorithm under high wind conditions. Two case studies of an extratropical cyclone and a polar low illustrated these new capabilities. The suggested geophysical model was also successfully used for AMSR-E successor AMSR2 on GCOM-W1 satellite which was launched on 18 May 2012 [22]. Though we still did not derive new calibration additions for this new instrument due to too little time of data availability, preliminary results of AMSR2 algorithm performance showed good correspondence with *in situ* measurements of sea surface wind speeds, even for high wind speed areas.

## 2. Modeling

### 2.1. Ocean Emission Model

Ocean emissivity for the calm ocean surface depends only on a dielectric constant of sea water. It is determined as one minus reflectivity, where the reflectivity can be accurately calculated from the Fresnel formula for a given water permittivity and a local incident angle. For the wind influenced surface the emissivity becomes a function of surface wind speed and direction. A calm sea surface is characterized by a highly polarized emission. Formulating a consistent theoretical model for the wind speed dependency on sea surface emissivity seems to be mostly complicated [23,24].

Three mechanisms can be named as responsible for the variation in the ocean emissivity with wind speed [25]. First, the appearance of the surface waves with wavelengths much larger than the microwave radiation wavelength mixes the horizontal and vertical polarization states and changes the local incidence angle. This phenomenon can be modeled as a collection of tilted facets, each acting as an independent specular surface [23]. The second mechanism is the sea foam, arising with wind speed more than 4–7 m/s. This mixture of air and water raises the emissivity for both polarizations. Sea foam models were developed in the past [26,27] and continue to be developed. So, complicated objects at the ocean surface, named integrally as “foam”, actually presents a mixture of foam, whitecaps, bubbles, spray, aerosol, and also water-biogenic and water-oil emulsions. All of these formations are modeled with serious difficulties because of their instability and microstructure variety [13,26]. Furthermore, the third roughness effect is the diffraction of the microwaves by surface waves, which are small compared to the radiation wavelength. Rice [28] was the first who provided the basic formulation for computing the scattering from a slightly rough surface. Some authors applied this scattering formulation to the problem of computing the emissivity of a wind-roughened sea surface, because these three effects can be parameterized in terms of the root mean square (rms) slope of the large-scale roughness, the fractional foam coverage, and the rms height of the small-scale waves. Each of these parameters depends on wind speed. The authors of [14,29–32] derived wind speed relationships for the three mentioned parameters, respectively. These wind speed relationships in combination with the tilt, foam and diffraction models provide the means to compute the sea-surface emissivity. Computations of such type have been done by many authors [9,14,33,34].

In addition to depending on wind speed, the large-scale rms slope and the small-scale rms height depend also on wind direction [34,35]. Another type of directional dependence occurs because the foam and capillary waves are not uniformly distributed over the underlying structure of large-scale

waves. The dependence of foam and capillary waves on the underlying structure produces an upwind-downwind asymmetry in the ocean surface emissivity [13]. The anisotropy of capillary and small gravity waves is responsible for the observed dependence of radar backscattering on wind direction. The upwind radar return is considerably higher than the crosswind return. These directional characteristics of the radar return have provided the means to sense wind direction from aircraft and satellite scatterometers [36].

So, well understood theoretical modeling of the ocean emission encounters serious difficulties in implementation. Numerical integration of complex equations needs simplifying assumptions, suggestions and parameterization.

The other approach exists to parameterize ocean emission wind dependency. This approach is associated with accurate measurements of the brightness temperature response to wind speed increase and derivation of the empirical relation between them as a function of incidence angle, sea surface temperature, salinity and wind speed. Most empirical ocean models are based on near-surface microwave radiance measurements to minimize the atmospheric constituent. Such coordinated observations were performed, for example, in [37] during the Fluxes, Air–Sea Interaction, and Remote Sensing (FAIRS) experiment. The results obtained during FAIRS showed a good agreement with previous models [11,23,24,38,39] and a good linear fit between the emissivity and surface wind speed in the range of 4–16 m/s at three incidence angles (45 °, 53 °, and 65 °) at 10.8 and 36.5 GHz. Slightly different results from [37] were obtained in [40]. Here, the isotropic (direction independent) wind induced emissivity for vertical and horizontal polarizations was derived by averaging globally over a large number of wind directions.

In the present study, two empirical wind speed dependencies were used for brightness temperature calculations. The first one already proved to be able to reproduce passive microwave wind dependency in the range of wind speeds up to 20 m/s. The Neural Networks algorithms for integrated atmospheric water parameter retrievals from SSM/I and AMSR-E measurement data were developed on simulated brightness temperatures. They were extensively validated against *in situ* data and led to significant (40%) retrieval accuracy increase [21]. This model will be referenced as Ros92, though actually it is the combination of several empirical wind induced emissivity models. For horizontal polarization the model of [39] is adopted. It is in the best agreement with all the models, referenced here, but provides the values of derivatives of the emissivity ( $\epsilon$ ) with respect to wind speed (WS)  $\partial\epsilon/\partial WS$  for the whole range of SSMIS and AMSR-E frequencies from 6 to 90 GHz. For vertically polarized  $\partial\epsilon/\partial WS$ , Ros92 uses a combination of [39] and [37] models. The main feature of Ros92 is an independence of  $\partial\epsilon/\partial WS$  from the wind speed. Many authors suppose [37,39,41,42] that the increase in the microwave emissivity with wind speed  $\partial\epsilon/\partial WS$  is a constant for the whole wind speed range (WS < 20 m/s). Their assumption is that the foam due to wave breaking at these winds does not change this constant. The value of  $\partial\epsilon/\partial WS$  is derived from the corresponding measurements which are usually restricted to a limited set of incidence angles and frequencies. Such models thus differ only by the value of  $\partial\epsilon/\partial WS$ . Earlier studies [39] tended to conclude approximately (dependent on frequency and angle) values of  $\partial\epsilon/\partial WS$  twice as low as the late models.

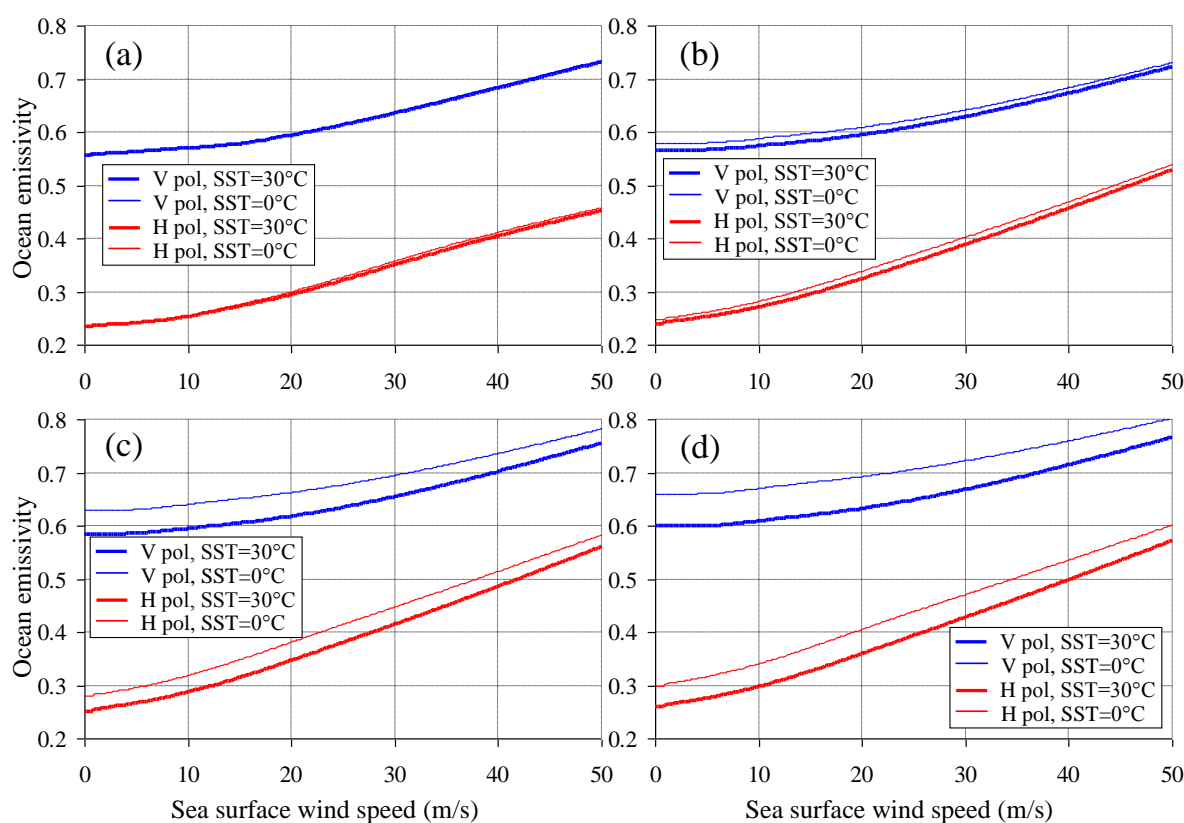
The second model for the wind induced emissivity comes from the experimental parameterization of  $\partial\epsilon/\partial WS$ , based on the work of Bertrand Chapron's team at IFREMER, Brest, France [43]. This team integrated *in situ* and satellite wind speed measurement data and built a high quality dataset of

consolidated ocean observations. The model will be referenced as Chapr12. According to Chapr12, ocean emissivity can be presented as a sum of the constituent, associated with the roughness changes, and the constituent, associated with the foam:

$$\varepsilon = \alpha \cdot (1 - f) + \beta \cdot f \quad (1)$$

where  $\alpha$  is a coefficient responsible for wind induced roughness and its influence on emission in terms of facet tilt wave diffraction,  $\beta$  is a coefficient responsible for all kinds of air-water mixtures in the form of foam, spray *etc.*,  $f$  is the fraction of the ocean covered by these mixtures. The foam fraction is mainly a function of wind speed, whereas  $\alpha$  and  $\beta$  are the functions of frequency, sea surface temperature, sea surface salinity, incidence angle, wind speed and polarization. The complex parameterization of  $\alpha$  and  $\beta$  is derived from numerous experimental studies [43]. For example, the resulting ocean emissivity—wind speed (WS) dependencies for AMSR-E channels at 10.65 and 18.7 GHz are shown in Figure 1a,b, where the upper curves refer to vertical, and lower ones—to horizontal polarizations. The incidence angle is constant and corresponds to that of AMSR-E  $-55^\circ$ ; the sea surface salinity is a constant of 34 ‰. The thicker lines refer to SST = 30 °C, the thinner lines refer to SST = 0 °C.

**Figure 1.** Ocean emissivity, calculated using Chapr12 model, as a function of sea surface wind speed  $WS$  for four lower AMSR-E frequencies: (a) 6.9 GHz, (b) 10.65 GHz, (c) 18.7 GHz, (d) 36.5 GHz. The thicker lines refer to SST = 30 °C, the thinner lines refer to SST = 0 °C. The upper (blue) curves are for vertical polarization, the lower (red) curves are for horizontal polarization.



The second important modeling of the ocean emission concerns the dielectric permittivity of water. A precise knowledge of the complex dielectric permittivity of water is essential for studying the transfer of the microwave radiation in the AOS. First, this parameter refers to the sea saline water and defines the sea surface emissivity and reflectivity, and, second, it refers to the fresh water of the cloud droplets. The most frequently used in the past model [44] is becoming increasingly inaccurate with the frequency increase [11,45]. A number of experimental studies of the last two decades [46–49] resulted in appearance of new updated models. Quite recently, a new permittivity model appeared [10] following the permittivity formulation of [47]. Its coefficients were determined by fitting the new permittivity measurement data, mostly important for L-band BT simulation (for MIRAS on SMOS and Aquarius on SAC-D instruments).

For presented geophysical model we adopted the model of [49] since it is extensively validated and valid for frequencies up to at least 90 GHz for the fresh water in the temperature range (including supercooled water) between  $-20\text{ }^{\circ}\text{C}$  and  $40\text{ }^{\circ}\text{C}$ , and for sea water for temperatures between  $-2\text{ }^{\circ}\text{C}$  and  $29\text{ }^{\circ}\text{C}$ . It should be noted that for radiometric simulation in L-band the model [10] should be used to account accurately for sea salinity variations.

## 2.2. Atmospheric Absorption Model

The atmospheric absorption in the microwave range of frequencies below 100 GHz is governed by three components: oxygen, water vapor, and liquid water in the form of clouds and rains [50]. The ice cloud influence on the brightness temperature is expressed only in signal diminishing due to scattering for higher frequency channels—for 85.5 GHz for SSMIS and for 89.0 GHz for AMSR-E. The sum of these three components gives the total absorption coefficient:

$$\alpha(h) = \alpha_{O_2}(h) + \alpha_{H_2O}(h) + \alpha_L(h) \quad (2)$$

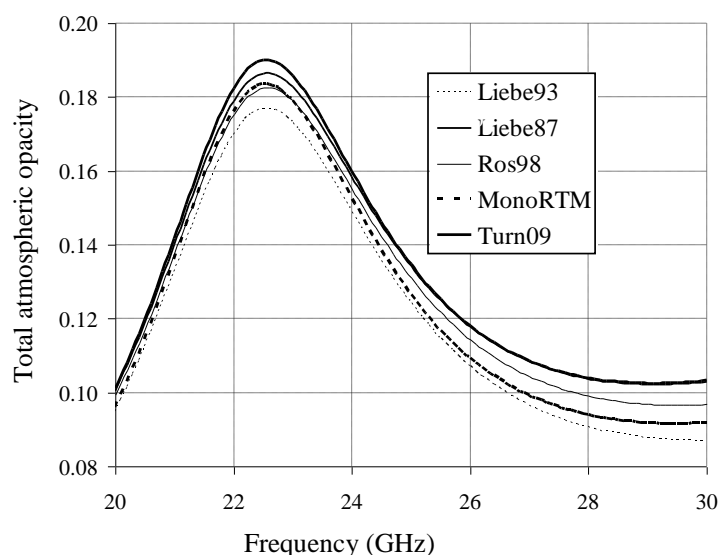
Each of the constituents in (2) depends on the atmospheric height  $h$ .

Since this work is based specifically on the consideration of the clear sky atmosphere to exclude all uncertainties of cloud modeling,  $\alpha_L = 0$ . Thus, liquid water absorption will not be considered here in detail. It may be taken from [40,51].

A lot of studies were devoted to the investigations of the oxygen and water vapor coefficient  $\alpha_{O_2}$  and  $\alpha_{H_2O}$  dependency on frequency ( $\nu$ ), atmospheric temperature ( $T$ ), pressure ( $P$ ), and water vapor density  $\rho$  [52–58]. In order to properly account for the radiative contribution of these gases, the radiative transfer models use the results of the accurate laboratory measurements of the parameters of their resonance lines (e.g., frequencies, strengths, half widths, shapes, temperature and pressure dependencies, *etc.*), currently available in common spectral databases (e.g., HITRAN [59]). These parameters are not perfect and vary from model to model. There are contributions in the far wings of the absorption lines, considered in most models as a “continuum” non-resonant absorption model. Improving the accuracy of the continuum absorption models has been an ongoing challenge for the radiative transfer community [57], especially for water vapor absorption. Some of the investigators adopt the parameters of a chosen spectral model and slightly modify either the strength of one or more lines or some other parameters. For example, Wentz [11] used [52] expressions with a reduced self-broadening component of the water vapor continuum.

Since the accuracy of the absorption model dramatically influences the radiative transfer modeling results, many studies inter compared different absorption models [57,60–63]. Such intercomparison is usually fulfilled for the downwelling radiation to minimize the errors associated with inaccurate estimation of the ocean constituent of the radiation. Clear sky conditions are also mandatory to minimize the ambiguities associated with liquid water content modeling in clouds. The aim of such work is always to select the model which best represents collocated in time and space radiometric measurements. At this stage, the quality of radiosonde measurements and radiometric calibration is estimated. One of the strongest conclusions of [57], confirmed also in [63], is that the original model of [54] does not match the observations at 150 or 31.4 GHz. Unfortunately, many groups are still using the water vapor continuum model from this model (e.g., the models in the intercomparison study of [62]).

**Figure 2.** Total atmospheric opacity  $\tau$ , calculated using Liebe87, Liebe93, Ros98, MonoRTM and Turn09 water vapor absorption models for a clear sky polar atmosphere ( $Q = 13.9 \text{ kg/m}^2$ ) for the frequency range 20–30 GHz. Liebe87 is used for oxygen absorption calculation in all calculations.



In this study, we used the same approach as described in [57]. The general difference is that instead of downwelling atmospheric radiation upwelling total atmosphere-ocean system radiation was estimated. Thus, we included the ocean constituent, described in the previous section, two atmospheric constituents and a little addition of cosmic radiation of 2.73 K [11].

We excluded [54] from the comparison in spite of its wide usage [57]. Four water vapor absorption models—[53] (Liebe87), [55] (Ros98), [64] (MonoRTM), and modified MonoRTM [57] (Turn09) and two oxygen absorption were used—[53] (Liebe87) and [58] (Tret05). The detailed description of each model can be found in the corresponding publications. Figure 2 shows the total atmospheric opacity  $\tau$  as a function of frequency  $\nu$  for the frequency range around water vapor resonance line at 22.235 GHz for a clear sky (total cloud liquid water content  $W = 0 \text{ kg/m}^2$ ) mid-latitude atmosphere (total atmospheric water vapor content  $Q = 13.9 \text{ kg/m}^2$ ). To calculate  $\tau$  we used five water vapor absorption models and Liebe87 model for oxygen absorption simulation for all five cases. The model of [54] (Liebe93) is included in Figure 2 to underline its underestimation of  $\tau$  around this water vapor spectral line.

We want to emphasize once more that the final goal of the current study was not the choice of the most correct molecular spectroscopy model for water vapor or oxygen absorption. The aim of the study was to find the combination of the atmospheric and oceanic models, simulating brightness temperatures for AMSR-E and SSM/I instruments in the best way, e.g. providing the least root mean square error (rms) between radiometric measurements and modeling results.

### 3. Data

#### 3.1. Satellite Passive Microwave Data

We used AMSR-E and SSMIS measured brightness temperatures for the selection of the most adequately performing geophysical model. We considered only those channels which are characterized by low ( $\leq 0.7$  K) values of noise (NE $\Delta$ T).

AMSR-E Level 1B swath data, consisting of calibrated brightness temperatures converted from observed sensor data of level 1A by the radiometric correction coefficients, were provided by Japan Aerospace Exploration Agency. AMSR-E made dual-polarization observations at the six frequencies: 6.925, 10.65, 18.7, 23.8, 36.5, and 89.0 GHz. From the altitude of 705 km, it measured the upwelling Earth brightness temperatures at about 55.0° Earth incidence angle with a resulting swath width of 1445 km. Earth observations are recorded at equal sample intervals of 10 km (5 km for 89.0 GHz channels) along the scan, though actual spatial resolution is worse for lower channels: from 15 km at 36.5 GHz to 50 km at 6.9 GHz. The sensitivity (noise equivalent temperature) for the channels from 10.65 up to 36.5 GHz is about 0.7 K and about 1.2 K at 89 GHz [65]. Sensor sensitivity and spatial resolution are the important factors to be taken into account when we compare radiometric measurements averaged over not only sample intervals but over much larger areas viewed by antenna lobes.

We used AMSR-E measurements at five lower frequencies (for both polarizations, in total 10 channels); two channels at 89 GHz were excluded from consideration. The brightness temperatures for the corresponding frequencies and polarizations will be denoted further as TB06H, TB06V, TB10H, TB10V, TB18H, TB18V, TB23H, TB23V, TB36H and TB36V.

SSMIS Level 1B swath calibrated brightness temperature data were downloaded from NOAA data center Comprehensive Large Array—Data Stewardship System [66]. The SSMIS collects microwave energy from the Earth's surface and atmosphere in 24 channels at frequencies from 19.35 to 183.31 GHz including those in the oxygen absorption band. The last allow air temperature profile retrievals [67]. Earth scene data for 24 channels are collected at 180 sample positions along the active portion of the scan in an angle of 143.2°. At the nominal orbital height of 833 km, this produces a swath width on the ground of 1707 km with 12.5 km scene spacing. The achieved scene width applies uniformly to all SSMIS channels. Then, for some channels several scenes are averaged to larger samples. This resampling reduces the effective noise for the cost of spatial resolution. We used 10 SSMIS channels for geophysical model selection and calibration: dually polarized measurements at 19.35, 37.0, and vertically polarized measurements at 22.235, 50.3, 52.8, 53.596, 54.40 and 55.5 GHz. The brightness temperatures for the corresponding frequencies and polarization will be denoted further as TB19H, TB19V, TB22V, TB37H, TB37V, TB50V, TB52V, TB53V, TB54V and TB55V.

### 3.2. Data for Brightness Temperature Calculations

Mostly reliable and accurate data on the geophysical parameters defining the microwave radiation of the system are needed for brightness temperature calculations.

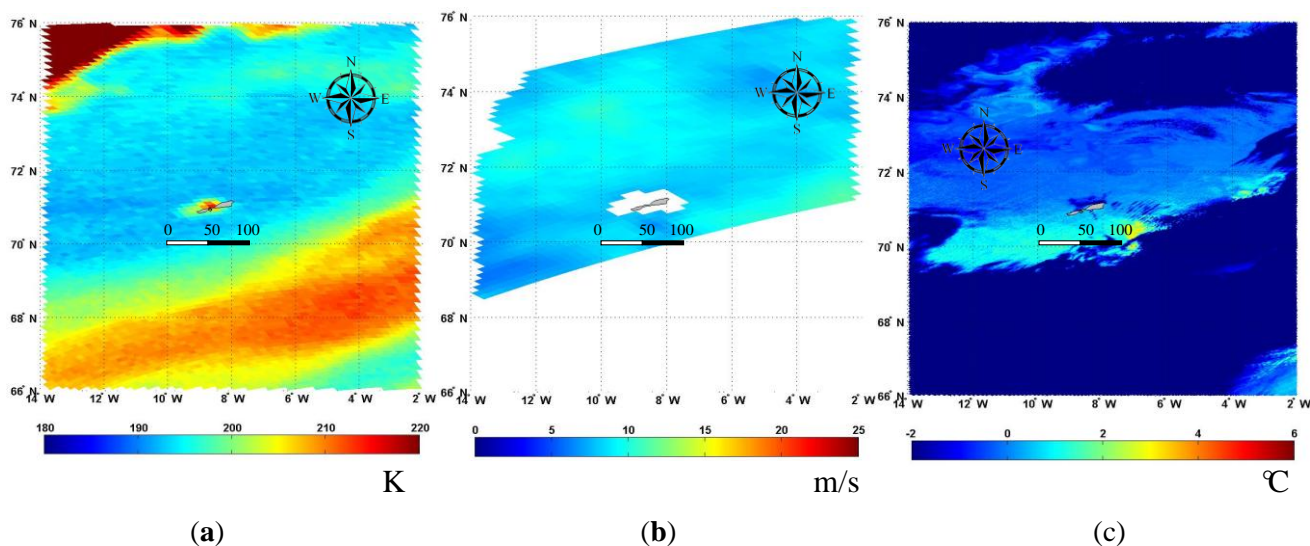
Model data (including re-analysis) are not appropriate for this task. This is not only due to insufficient accuracy but also due to not enough specification for the whole atmospheric height. The brightness temperature calculations can be compared with satellite radiometric measurements only if the atmospheric meteorological parameters are known at detailed height levels beside the main isobar surfaces. Their values are especially important near the surface with high values of atmospheric humidity. Radiosonde data from meteorological stations satisfied these requirements. The data from Wyoming University [68] contain more than 40 levels from the Earth surface up to relative humidity of about 10% (height more than 25–30 km). The next restriction, which should be applied to radiosonde stations, is the station level over the sea. In case of a comparatively large height of the station, the extrapolation of the air temperature and humidity profiles is needed for correct brightness temperature calculations. The next consideration concerns the temporal-spatial collocation of the measurements in a point (atmospheric pressure, air temperature, air humidity) and over the pixel. Meaning nonzero time difference in measurements and spatial remote sensing averaging over antenna field of view, radiometric BT should be temporally and spatially homogeneous to be comparable with simulated BT. This is especially important for the channels sensitive to atmospheric meteorological parameters. Since we impose the absence of clouds, this means that the channels around the water vapor absorption line of 22.235 GHz and in the oxygen band of 50–60 GHz should be homogeneous in time and space. It is almost impossible to implement such a requirement in the regions with high air humidity, e.g., at tropic latitudes. We used two polar stations—Jan Mayen (#01001: 70.93N; 8.67W, 9 m over the sea level) and Bjornoya (#01028: 74.51N; 19.01E, 18 m over the sea level) in the Norwegian and Barents Seas correspondingly—as the radiosonde data source for several more reasons. First, high latitude ensures high temporal resolution of radiometric data due to polar orbits of DMSP and Aqua. This enables not only to choose the data with minimum time difference between satellite and radiosonde measurements but also to check their time homogeneity. Second, since the radiosonde stations usually provide data twice a day it is most important to have the radiometer data close to either 0:00 UTC or 12:00 UTC. Both SSMIS on F16 and AMSR-E on Aqua have paths over both stations around 12:00 UTC  $\pm$  4 hours. Furthermore, the third reason concerns the availability of wind speed data for model calculations. We used scatterometer wind speed fields from MetOp-A ASCAT as the wind speed source data in numerical calculations of brightness temperatures. We suppose that spatially averaged fields of this parameter are more meaningful than *in situ* wind speed measurements in a point, e.g., buoy data. Scatterometer data seem to be most appropriate since they have approximately the same spatial resolution as the data of passive microwave radiometers. Metop-A ASCAT data perfectly fit the task also due to the time passage over Jan Mayen and Bjornoya stations around midday. The data of scatterometer SeaWinds on QuikSCAT satellite cannot be used due to night and evening passage over the stations with large time difference for time collocation. That is why we selected data only starting from March 2009, when Metop-A ASCAT wind fields became available.

We checked the absence of clouds by two ways. First, we selected only those radiosondes where the relative humidity did not exceed 70% along the whole humidity atmospheric profile. This ensured that

no clouds could form under such threshold. Then, for these selected radiosondes we analyzed Aqua MODIS images to check and ensure the absence of clouds not only over the station but also over comparatively large area taking into account nonzero time difference in the measurements of different kinds and spatial averaging. These clear sky MODIS data presented the most suitable source of sea surface temperature (SST) data for the brightness temperature calculations. The values of sea surface salinity (SSS) were taken from the World Ocean Atlas [69]. Since we did not calibrate L-band channels we did not need more precise salinity knowledge.

We selected about 150 data, satisfying all the above mentioned requirements. These data consisted of cloudless 12-hour radiosonde profiles of atmospheric air temperature, humidity and pressure from Jan Mayen and Bjornoya stations, collocated in time with MetOp-A ASCAT wind fields, DMSP F16 SSMIS and Aqua AMSR-E homogeneous brightness temperature fields within 2 h time difference, Aqua MODIS SST and World Ocean Atlas SSS. The wind speed range for the selected data is 0–30 m/s. The distance from the station to a radiometer/scatterometer pixel was within the limits of 70–120 km to exclude land influence and be not far away from the radiosonde. We checked the homogeneity of the atmosphere by the analysis of brightness temperature fields for the channels at 22.235 and 23.8 GHz, vertical polarization for SSMIS and AMSR-E instruments correspondingly. We selected only those data where BT variations within the collocation distance did not exceed the value of  $NE\Delta T$ . When the brightness temperature homogeneity spread far away from the station we considered it possible to use several scatterometer/radiometer/spectroradiometer collocations to enlarge the data set by additional ocean surface data (wind speed and SST) for the same atmosphere. Figure 3 illustrates an example of satellite data fields qualified as appropriate for the calculations. Cloudless area is located in the upper left of the images. Mesoscale variations of TB23V are seen in Figure 3a. Surface wind speed variations are within 2–3 m/s (Figure 3b). Clouds cover the bottom right side of the images. They are characterized by the high TB23V values and low cloud top temperature (Figure 3c). SST increases from the North ( $-1\text{ }^{\circ}\text{C}$ ) to the South ( $+1\text{ }^{\circ}\text{C}$ ).

**Figure 3.** Satellite data fields taken over Jan Mayen radiosonde station on 3 May 2011: (a) Aqua AMSR-E brightness temperature at 23.8 GHz, vertical polarization, 12:28 UTC; (b) MetOp ASCAT wind speed, 13:34 UTC; (c) Aqua MODIS SST, 12:30 UTC



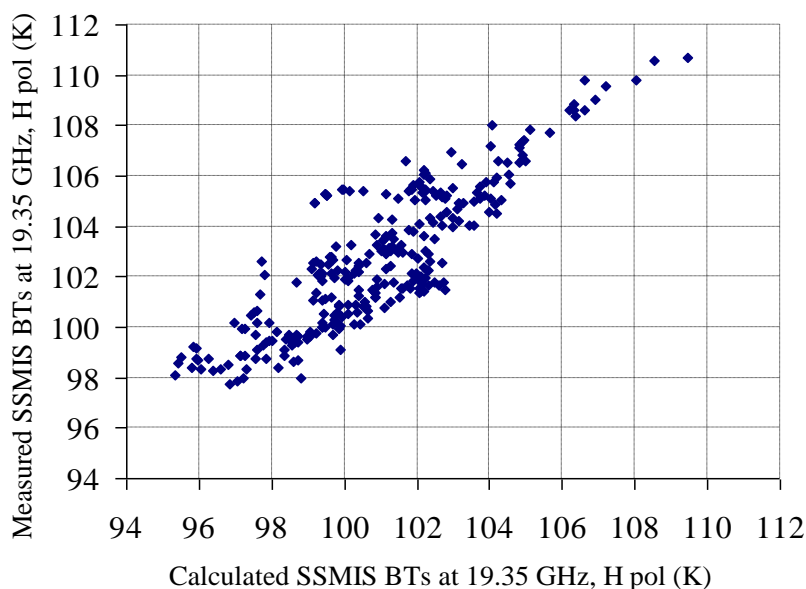
#### 4. Results and Discussion

We used the selected data to calculate brightness temperatures for AMSR-E and SSMIS instrument characteristics (incidence angle, selected frequencies and polarizations). We calculated BT using four models for water vapor absorption—Liebe87, Ros98, MonoRTM and Turn09, 2 oxygen absorption models Liebe87 and Tret05, two ocean emission wind dependency models: Ros92 and Chapr12, and a single sea water (or saline water) permittivity model of [49]. We then compared the calculated values of brightness temperatures with radiometric measurements for AMSR-E for the channels at 6.925, 10.65, 18.7, 23.8 and 36.5 GHz at both polarizations and for F16 SSMIS for the channels at 19.35 and 37.0 GHz at both polarizations, and at 22.235, 50.3, 52.8, 53.596, 54.4 and 55.5 GHz for only vertical polarization.

As it could have been presumed, the general difference between the models manifested in the channels corresponding to the frequencies close to water vapor or oxygen spectral lines or band. So, there were no differences between the two oxygen absorption model performances on the channels other than at frequencies higher than 50 GHz. Also, any water vapor absorption model can be used to calculate brightness temperatures in the band of 50–60 GHz with no significant difference.

For each of the 10 channels for each instrument, the resulting scatter plot of measured *versus* simulated brightness temperature values was built and the corresponding statistical analysis was fulfilled. An example of such a scatter plot for SSMIS TB19H is shown in Figure 4. It can be noticed that the data are rather scattered. Since the brightness temperature fields at the channels, sensitive to water vapor content, are selected to be uniform around the station, it may be supposed that the scatter is caused by the variability, time difference and errors in the wind speed fields given by ASCAT.

**Figure 4.** DMSP F16 SSMIS brightness temperatures measured at 19.35 GHz, horizontal polarization *versus* calculated brightness temperatures using Turn09 model for water vapor absorption, Liebe87 model for oxygen absorption and Chapr12 model for ocean emission wind dependency model calculations.



The resulting root mean square differences are given in Tables 1–3 for SSMIS and AMSR-E. We included only significant results, e.g., only those models are listed which influence rms. For example, due to strong atmospheric absorption in the oxygen absorption band (sounding SSMIS channels) ocean emission model differences are negligible comparatively to the oxygen absorption model differences.

Table 1 summarizes the results, relating to the oxygen model performance for the five SSMIS channels in the oxygen band. It can be seen that for these two models rms between measured and calculated brightness temperatures are both close to each other and small in value. The maximum difference of 0.22 K between rms is observed for TB55V channel. The other differences in rms do not exceed 0.08 K. Such close results indicate that in spite of different complexity (Liebe87 model accounts for 48 oxygen lines and Tret05—only for 40 lines) and different types of temperature and pressure oxygen coefficient dependence both models lead to identical results. Moreover, Tret05 model was extensively validated for a wide range of temperatures [70] whereas Liebe87 model was validated only for positive temperatures. The fact that the data set used in the study is featured by lower temperatures due to the polar station source did not influence Liebe87 model performance. Since the data included significantly varied atmospheric pressure profiles (ground level pressure varied from 970 to 1020 mB) it can be concluded also that the pressure dependence of the oxygen absorption coefficient is parameterized properly. Resuming the analysis of Liebe87 and Tret05 oxygen absorption model performance, we state that such low differences in rms imply that any of these models can be successfully used in brightness temperature simulations without losing accuracies.

The other general conclusion that can be drawn from Table 1 relates to the instrument performance. All considered SSMIS oxygen band channels are well calibrated and the calibration is stable for 2009–2011 period of time (time period covered by the data).

**Table 1.** Root mean square difference (in K) between simulations and measurements for Liebe87 and Tret05 models used for the oxygen absorption at SSMIS oxygen band channels. Turn09 is used for water vapor absorption.

	TB50V	TB52V	TB53V	TB54V	TB55V
Liebe87	0.46	0.57	0.84	0.56	0.88
Tret05	0.51	0.59	0.92	0.58	1.10

Analyzing rms for SSMIS window channels, summarized in Table 2, we can see that the difference in five water vapor absorption model performances is in accordance with those reported in [57] except that rms values in our study are 0.5–1 K larger than in the cited paper. Since in [57] a ground-based two channel microwave radiometer (23.8 and 31.4 GHz) with well controlled calibration was used for measuring downwelling radiation, these systematic (through all models) differences can be definitely referred to calibration issues. The rms at the TB22V channel—the channel with the closest to a water vapor line of 22.235 GHz—is not significantly different from the other channel rms. This allows concluding independency of model performance on the total atmospheric water vapor content (TWV), though restricted to 32 kg/m<sup>2</sup> (the maximum TWV in the data set). Contrarily to [57], we did not obtain the results indicating worse performance of Liebe87 model comparatively to the other models.

**Table 2.** Root mean square difference (in K) between simulations and measurements for eight model combinations for SSMIS lower frequency channels. Liebe87 is used for oxygen absorption.

		TB19H	TB19V	TB22V	TB37H	TB37V
WV	Turn09	1.42	1.21	1.25	1.28	0.76
OE	Chapr12					
WV	Ros98	1.50	1.32	1.40	1.31	1.20
OE	Chapr12					
WV	MonoRTM	1.49	1.32	1.27	1.30	0.81
OE	Chapr12					
WV	Liebe87	1.43	1.23	1.38	1.30	0.95
OE	Chapr12					
WV	Turn09	1.62	1.43	1.55	1.47	1.10
OE	Ros92					
WV	Ros98	1.67	1.48	1.62	1.52	1.40
OE	Ros92					
WV	MonoRTM	1.65	1.47	1.58	1.51	1.20
OE	Ros92					
WV	Liebe87	1.64	1.44	1.60	1.51	1.30
OE	Ros92					

The same conclusion follows from the Table 3 relating to the window channels of AMSR-E instrument. A possible explanation can be related to the principle difference between the studies: in [57] downwelling radiation is calculated and measured. In the present work, upwelling radiation is considered with significant constituent of the ocean radiation. In this case, ocean emission correct modeling becomes more important for the comparisons between calculated and measured brightness temperature values. Also, the accuracy of the wind speed used in calculations can have crucial significance for the results. That is why the data set used in the study is restricted not only by the absence of clouds but also by availability of ASCAT wind data over the station with minimal time difference between radiosounding, satellite and ASCAT measurements.

Moreover, as it might be presumed, we can see also from Table 3 that the choice of water vapor absorption model does not at all influence the comparison results for the lower AMSR-E frequencies in C- and X-bands (TB06H, TB06V, TB10H, TB10V)—far away from the water vapor line center. Instead, the results in Table 2 show that the choice of the ocean emissivity model acquires the critical meaning. Chapr12 model for ocean emissivity provides better results in comparison to the Ros92 model. For 19, 22 and 37 GHz channels, the Chapr12 rms values are less than the Ros92 rms values on 0.2–0.5 K. The main reason is the usage of the new experimentally-derived wind speed emission dependence in which  $\partial\varepsilon/\partial WS$  derivative is approximately two times larger than that used in the Ros92 model [39].

The same conclusion can be deduced from Table 3 for AMSR-E window channels. The differences in rms values reach 0.8–0.9 K. For 6 and 10-GHz channels—the main channels providing the principal contribution in Sea Surface Temperature (SST) and WS retrievals—these differences are equal to  $\approx 0.4$  K. This means that the use of Chapr12 model will provide more accurate retrieval of SST and

WS: SST rms error decrease ensured by 0.4 K will be  $\approx 0.7$ – $0.8$  K and the corresponding WS rms error decrease will be  $\approx 0.3$ – $0.4$  m/s.

**Table 3.** Root mean square difference (in K) between simulations and measurements for 8 model combinations for AMSR-E lower frequency channels. Liebe87 is used for oxygen absorption.

		TB06H	TB06V	TB10H	TB10V	TB18H	TB18V	TB23H	TB23V	TB36H	TB36V
WV	Turn09	0.83	0.70	0.91	0.78	1.14	0.77	1.94	1.08	1.22	0.65
OE	Chapr12										
WV	Ros98	0.84	0.71	0.91	0.79	1.21	0.93	2.60	1.50	1.42	0.90
OE	Chapr12										
WV	MonoRTM	0.83	0.71	0.91	0.78	1.20	0.90	2.40	1.48	1.38	0.87
OE	Chapr12										
WV	Liebe87	0.83	0.70	0.92	0.79	1.16	0.79	2.00	1.10	1.23	0.69
OE	Chapr12										
WV	Turn09	1.11	1.00	1.30	1.22	1.40	0.92	2.15	1.30	1.43	0.95
OE	Ros92										
WV	Ros98	1.12	1.11	1.32	1.25	1.48	1.20	3.20	1.96	1.56	1.43
OE	Ros92										
WV	MonoRTM	1.11	1.11	1.31	1.24	1.47	1.10	3.15	1.90	1.52	1.35
OE	Ros92										
WV	Liebe87	1.12	1.1	1.35	1.24	1.46	0.94	2.18	1.35	1.47	1.10
OE	Ros92										

It is very likely that this difference will be increased at high wind speeds. Unfortunately, there are no hurricane-force data in our data set for well grounded confirmation of this statement. However, we provided an indirect confirmation by the analysis of high wind speed events in Section 5. We present there the application of the new geophysical model to AMSR-E wind speed retrieval algorithm development and verify better performance of the new algorithm in high wind areas by means of the comparison with other WS products.

Fortunately, the obtained results did not raise the questionable problem of choosing the criteria for the selection of the best model selection in case of different behavior of rms at different radiometric channels.

The results demonstrated the least root mean square difference between simulations and measurements for all considered radiometric channels provided by Turn09 model for water vapor absorption (WV), Liebe87 model for oxygen absorption (OX) and Chapr12 model for ocean emission wind dependency (OE) model calculations. That fact that a single model combination ensured the best results for both radiometers, allows concluding that this model combination can be used not only for considered instruments but for other passive microwave radiometers including AMSR2. We are collecting the similar data for AMSR2 calibration currently.

The obtained statistic for the best model combination for all considered channels is presented in Tables 4 and 5 for AMSR-E and F16 SSMIS correspondingly.

It follows from Tables 4 and 5 that the maximum difference between measured and computed brightness temperatures can reach 5–6 K for F16 SSMIS and 4–6 K for AMSR-E. The cases with maximum differences should be analyzed in details to explain such large values. It is not inconceivable that the maximum observed differences (at 19 and 37 GHz frequencies, horizontal polarization) are due to the local features associated with the sea surface, and the maximum observed difference

at 53 GHz, vertical polarization might be caused by the lower troposphere variability over the radiosounding station.

**Table 4.** Descriptive statistics of the differences between measured and calculated brightness temperatures for DMSP F16 SSMIS instrument for cloudless atmosphere. The atmosphere-ocean geophysical model is comprised of Turn09 model for water vapor absorption, Liebe87 model for oxygen absorption and Chapr12 model for ocean emission wind dependency.

	TB19H	TB19V	TB22V	TB37H	TB37V	TB50V	TB52V	TB53V	TB54V	TB55V
mean, K	1.76	1.37	0.80	1.93	-2.03	-0.63	1.34	4.54	1.55	0.99
rms, K	1.42	1.21	1.25	1.28	0.76	0.46	0.57	0.84	0.56	0.88
minimum, K	-1.29	-1.17	-2.89	-1.06	-4.08	-2.05	0.04	2.46	0.25	-1.05
maximum, K	5.79	5.11	4.04	5.14	-0.16	0.45	2.61	6.26	2.63	2.64

**Table 5.** Descriptive statistics of the differences between measured and calculated brightness temperatures for Aqua AMSR-E instrument for cloudless atmosphere. The atmosphere-ocean geophysical model is comprised of Turn09 model for water vapor absorption, Liebe87 model for oxygen absorption and Chapr12 model for ocean emission wind dependency.

	TB06H	TB06V	TB10H	TB10V	TB18H	TB18V	TB23H	TB23V	TB36H	TB36V
mean, K	1.10	0.56	-0.09	-0.09	0.28	-0.21	0.90	0.67	-3.81	-4.07
rms, K	0.83	0.70	0.91	0.78	1.14	0.77	1.94	1.08	1.22	0.65
minimum, K	-0.79	-0.80	-2.32	-1.81	-2.24	-1.75	-4.14	-1.95	-6.27	-5.71
maximum, K	3.00	2.40	1.72	2.07	2.66	2.43	4.24	3.07	-0.55	-2.37

Obtained mean differences can be used as model/calibration additions to adjust simulated brightness temperature values to instrumentally measured BT. They also serve as a facility to use modeling data for geophysical parameter retrieval algorithm development.

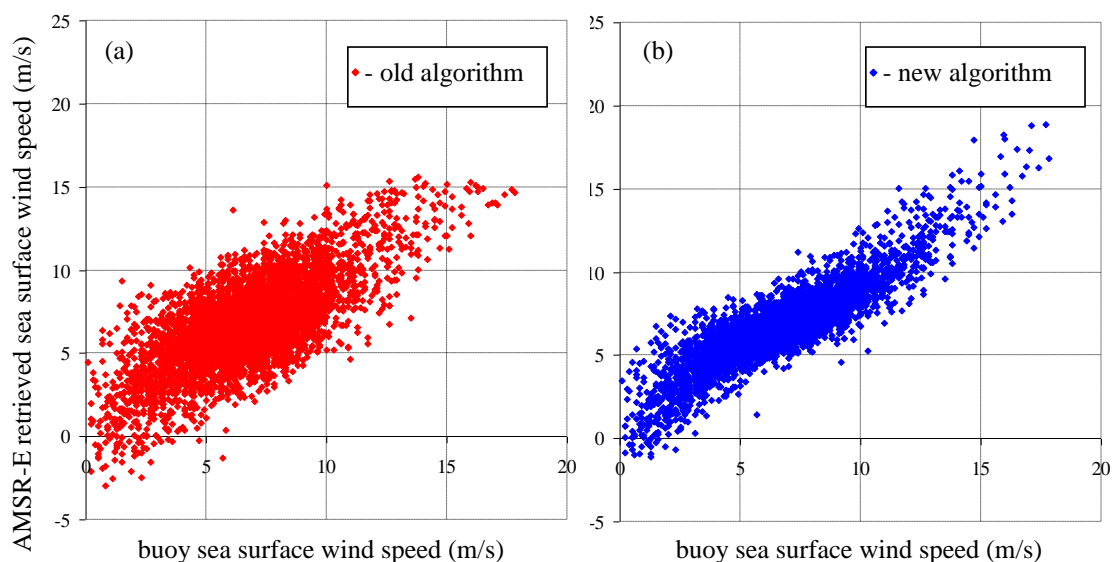
We also studied the dependence of the estimated differences on such determinative for brightness temperature parameters, as sea surface wind speed and total atmospheric water vapor content. We found no significant dependence of measured/simulated difference on wind speed either for SSMIS or for AMSR-E for any of the considered instrument channels. Nevertheless, it is obvious that a wider range of total water vapor content conditions, than ensured by two polar stations and presented in the study, would be more representative for the general model validation. An increased data base for the broader range of environmental parameters should be used to compute brightness temperatures and compare them with measured ones to confirm the obtained results. More accurate modeling and retrieved geophysical parameter values have especial importance for climatic research.

## 5. Model Application

To demonstrate the applicability of an updated geophysical model, we used it (along with brightness temperature corrections) to develop the new algorithm for sea surface wind speed retrievals from AMSR-E measurement data. The methodology for the algorithm development is described in

detail in [21]. First, we carried out the simulations of the brightness temperatures for the input data sets of atmospheric meteorological parameter profiles and ocean surface parameter data (sea surface temperature, salinity and wind speed). These simulations were performed for frequencies, polarization, sensitivity, and sensing geometry of AMSR-E instrument. Then, the Neural Network function was trained on the dataset of simulated brightness temperatures for sea surface wind retrievals. We found that the usage of four lower frequency AMSR-E channels (6H, 6V, 10H, 10V) ensured the least retrieval error and the most stable algorithm performance practically independent on weather conditions. The algorithm details are beyond the scope of this paper but we summarize here the validation results. The algorithm was validated using Japan Aerospace Exploration Agency (JAXA) database of more than 15,700 collocated AMSR-E and buoy wind speed measurements with the total retrieval error of about 1.2 m/s for the algorithm using a new geophysical model and about 2.7 m/s for the algorithm using an old one, described in [21]. The data were spatially collocated within 50 km distance from the buoy locations. Time difference was less than 1 hour. The corresponding scatter plots of AMSR-E retrieved *versus* buoy wind speeds are shown in Figure 5a for the old algorithm and in Figure 5b for the new one.

**Figure 5.** Scatter plots of AMSR-E retrieved WS *versus* buoy measured WS: (a) the algorithm is trained using brightness temperature calculations with an old geophysical model [21], (b) the new algorithm.

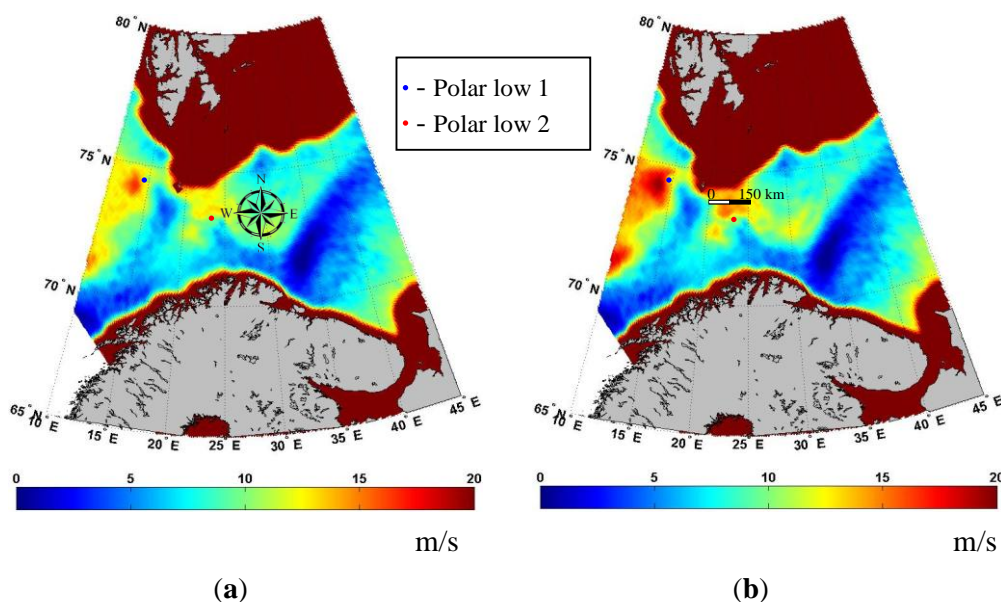


We can observe the worst performance of both algorithms for the range of very low (<2 m/s) sea surface wind speeds. This can be explained by the low accuracies of either buoy measurements or ocean emissivity wind speed dependence for this range. However, besides the overall larger scatter of the data in Figure 5a comparatively to Figure 5b, we can see that the new algorithm performs with no significant bias at the range of wind speeds higher than 15 m/s. The old WS algorithm clearly underestimates WS values for high winds. This is the crucial advantage of the new AMSR-E sea surface wind speed retrieval algorithm. Exactly this feature—ability to perform with high accuracy for the areas of high winds—allows using this algorithm to study dangerous high wind events in which

wind speed can reach storm and hurricane force values. Below, two examples of such events—a system of polar lows in the Barents Sea and an extratropical hurricane system over the North Atlantic—are considered.

The first example of the algorithm application is shown in Figure 6 showing the wind speed field developed in a polar low system in the Barents Sea. This figure shows two polar lows developed on 12 March 2011 in the Barents Sea and manifesting themselves in the wind vortex structures with high wind speed areas ( $WS > 12$  m/s). WS field on the left (Figure 6a) is retrieved with the old algorithm, whereas WS field on the right is retrieved with the new algorithm. It can be seen that the new algorithm provides higher wind speed estimates over the polar low areas than the old algorithm.

**Figure 6.** Polar lows 1 and 2 in the Barents Sea on 12 March 2011 at 9:56 UTC. Sea surface wind speed was derived from Aqua AMSR-E measurement data with Neural Network algorithms: (a) the algorithm is trained using brightness temperature calculations with an old geophysical model [21], (b) the new algorithm. The dark red areas indicate ice covered regions and coastal zone with strong land contamination where the retrievals are not possible.



The considered polar lows (PLs) were not marked on the surface analysis charts for 06 and 12 UTC on 12 March 2011 issued by UK Meteorological Office [71]. This is typical for mesoscale lows with the size less than approximately 200 km. Polar lows are small sized extreme weather events, characterized by high wind speeds and very fast development. Their life cycle may be as short as only 12 h. That is why it is always a problem to compare the wind fields in PLs estimated by different satellite instruments in different times even if time difference constitutes only 1–2 h. For example, for the considered polar low system Metop-A ASCAT wind fields were taken 2.54–4 h later when the system state had changed significantly comparatively to the moment of AMSR-E measurements. Fortunately, we had an Envisat ASAR image of the PL 2 (Figure 7b) with a time difference between AMSR-E measurements of only half an hour. This difference is nevertheless large enough for polar lows so not to allow wind field difference analysis. Indirect conclusion about the algorithm

performance can only be done estimating the maximum wind speeds developed in the cyclone. The maximum WS retrieved from AMSR-E with the new algorithm for the PL 2 is about 18 m/s, which is in better correspondence with a maximum WS of 20 m/s retrieved from the Envisat ASAR image of the PL 2 (Figure 7b). The maximum WS in case of the old algorithm usage is only about 14 m/s.

**Figure 7.** (a) Envisat ASAR image, taken on 12 March 2011 at 9:25 UTC and (b) Sea surface wind field retrieved from this image (image courtesy of CLS SOPRANO).

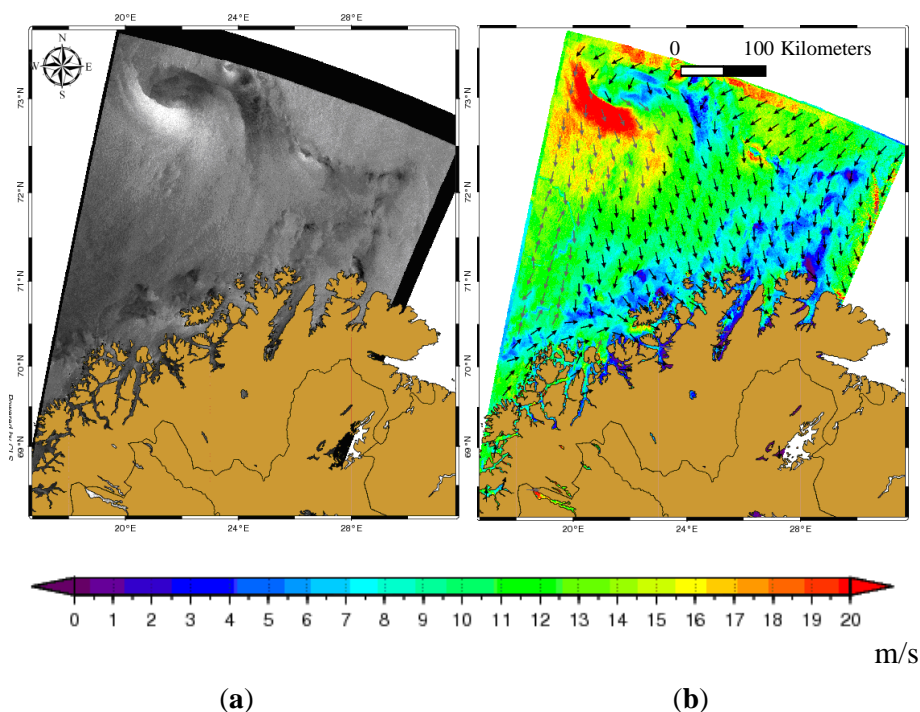
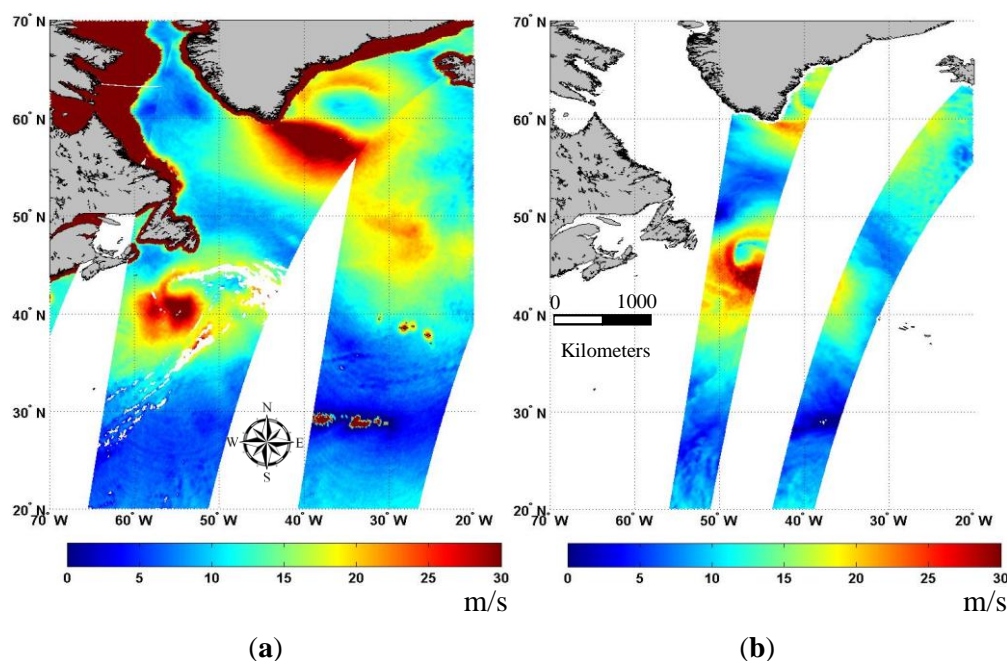


Figure 8 demonstrates the possibilities of the new algorithm to estimate high wind speeds in the areas of extratropical cyclones. AMSR-E retrieved wind speed fields associated with the two extratropical cyclones over the North Atlantic on 13 February 2011 are shown in Figure 8a as compared with the Metop-A advanced scatterometer (ASCAT) Level 2 Operational and Optimized Coastal Ocean Near-Real-Time ocean wind vector product in Figure 8b. One of the most powerful extratropical storms Quirin is the cyclone south-west of Newfoundland, less intensive cyclone is the storm Paolini also with hurricane-force winds blowing south of Greenland. The maximum wind speed over Paolini (41 m/s) at the moment of AMSR-E measurements was greater than the maximum wind speed over Quirin (36 m/s). The absence of precipitation and strong convective clouds, leading to low values of the atmospheric absorption near the south-east coast of Greenland, allowed WS retrievals over the whole Paolini area. Quirin system was the last of four deep lows with hurricane-force winds that developed in close succession over the North Atlantic. Quirin cyclone was considered in detail in [72], where the necessity to use different satellite data to provide a comprehensive analysis is stressed. A lot of data from different sources were collected to observe the dynamics of these storms, including those from scatterometer and altimeter instruments. At the moment of AMSR-E measurements, a part of this system was covered with optically thick atmosphere, making WS retrievals not possible (white areas in the Figure 8a). Again, the time difference between ASCAT and AMSR-E measurements is too large (more than 7 h) to make the direct pixel to pixel comparison between sea surface wind speed retrieved

values. However, as in the previous case, we can indirectly estimate the ability of the new algorithm to obtain high wind speeds comparable with other WS products. The maximum AMSR-E wind speed is about 36 m/s 7 h earlier than ASCAT measurements with a maximum WS of 34 m/s. Altimeter data (significant wave height) confirmed the hurricane-force winds for Quirin. It is emphasized in [72] that the actual maximum wind speed estimates are very difficult to obtain and validate with *in situ* measurements. However, the general agreement of all sensor estimations, including AMSR-E retrieved wind speeds, up to hurricane-force winds is remarkable.

**Figure 8.** Sea surface wind speed fields for the two extratropical cyclones over the North Atlantic on 13 February 2011: (a) AMSR-E retrieved WS at ~4–7 UTC; (b) Metop-A ASCAT Level 2 Operational and Optimized Coastal Ocean Near-Real-Time ocean wind vector product at ~12:30 UTC.



These two case studies demonstrated the adequate performance of the new AMSR-E WS retrieval algorithm and new possibilities associated with wind speed estimation under high wind conditions.

## 6. Conclusion

In this study, we modeled brightness temperatures (BT) over open oceans under non-precipitating conditions for two satellite instruments—for Advanced Microwave Sounding Radiometer—Earth Observing System (AMSR-E) onboard Aqua satellite and for Special Sensor Microwave Imager/Sounder (SSMIS) onboard F16 satellite of Defense Meteorological Satellite Program (DMSP). We simulated BT using different combinations of existing atmospheric absorption and ocean emission models. We then compared the calculated values of BTs with collocated in time and space satellite measurements under cloudless conditions. On the basis of this comparison, we made a choice of the best model combination, providing the least root mean square difference between the calculations and measurements. We also obtained the adjustments to simulated BT values accounting cumulatively for geophysical model ambiguities and sensor calibration errors. We performed the calculations for the

data set of simultaneous clear sky measurements of the atmospheric and oceanic parameters. The comparison was done for F16 SSMIS channels at 19.35 and 37.0 GHz at both polarizations, and at 22.235, 50.3, 52.8, 53.596, 54.40 and 55.5 GHz for only vertical polarization and for AMSR-E for the channels at 6.925, 10.65, 18.7, 23.8 and 36.5 GHz at both polarizations.

The results showed that the water vapor absorption model described in [57] (Turn09), the oxygen absorption model described in [53] (Liebe87) and the ocean emission wind dependency model described in [43] (Chapr12) ensured the least root mean square error (rms) between the simulations and measurements. This combination of models ensured the best results for all considered radiometric channels.

We obtained the results indicating similar performance of considered oxygen absorption models [53,67]. This allowed concluding that any of them could be successfully used in brightness temperature simulations without losing accuracies. Analyzing rms, we have also postulated effectively the calibration of all considered SSMIS oxygen band channels stable for the 2009–2011 period of time.

When we considered water vapor absorption model performances for SSMIS and AMSR-E window channels, we found systematic (for all models) differences between calculated and measured BTs. This can definitely be referred to as a calibration issue. We also did not obtain the results indicating worse performance of the Liebe87 model [53] comparatively to the other models which had been reported in [57]. We found the best performance for the model Turn09 [57], its performance independent of the total atmospheric water vapor content, though restricted to 32 kg/m<sup>2</sup>—the maximum in the data set.

The obtained results suggest that for the simulation of the BT of the atmosphere-ocean system, the choice of the correct ocean emission model becomes much more important than for already well-established oxygen and water vapor absorption models. We found that the Chapr12 model [43] for the ocean emissivity provided better results in comparison to the Ros92 model [39] for all considered AMSR-E and SSMIS channels. For 19.35, 22.235 and 37 GHz SSMIS channels, the Chapr12 rms values are less than Ros92 rms values on 0.2–0.5 K. For AMSR-E channels, these differences constitute 0.4 K for 6.9 and 10.65 GHz channels and 0.80–0.9 K for 18.7, 23.4 and 36.5 GHz channels.

We obtained mean differences between the simulations and measurements which can be used to convert modeled BT to measured BT. These differences, presented in Tables 4 and 5, can be used to remove model/calibration inconsistencies.

We demonstrated the application of the suggested model by means of the development of the new algorithm for sea surface wind speed (WS) retrievals from AMSR-E data. We validated this algorithm using a database of collocated in time and space AMSR-E and buoy wind speed measurement data. The validation results showed that the total retrieval error was 1.2 m/s for the algorithm using a new geophysical model and 2.7 m/s for the algorithm using an old one [21].

We showed that the old WS algorithm underestimated wind speeds for high winds. We stated the ability of the new WS algorithm to be used to study dangerous high wind events, illustrating this by two case studies and showing adequate AMSR-E algorithm performance under high wind conditions. However, more quantitative analysis including hurricane-force winds is needed to substantiate this claim.

We suppose that a considered geophysical model along with the calibration adjustments can be used in any research associated with BT modeling and following algorithm development. With this, a wider

range of total water vapor content conditions should also be used to extend the validation of the model for tropical latitudes.

### Acknowledgments

Funding for this research was provided by the Mega-grant of the Russian Federation Government to support scientific research under the supervision of leading scientist at RSHU, No. 11.G34.31.0078, Russian Fond for Basic Research Project 13-05-12093-ophi-m and Japan Aerospace Exploration Agency Project F10. This research was also supported by the European Space Agency (ESA) Support to Science Element (STSE) project OceanFlux-Greenhouse Gases (contract 4000104762/11/I-AM).

### Author Contributions

Elizaveta Zabolotskikh is a researcher conducting calibration study, all programming, calculations, comparison and development of retrieval algorithms. She is also responsible for figures and general text. Leonid Mitnik took part in the forward modeling, literature review and analysis. Bertrand Chapron is the originator of the wind speed emissivity model. He also took part in all discussions and analysis at all the stages of the research.

### Conflicts of Interest

The authors declare no conflict of interest.

### References

1. Bell, W.; Candy, B.; Atkinson, N.; Hilton, F.; Baker, N.; Bormann, N.; Kelly, G.; Kazumori, M.; Campbell, W.F.; Swadley, S.D. The assimilation of SSMIS radiances in numerical weather prediction models. *IEEE Trans. Geosci. Remote Sens.* **2008**, *46*, 884–900.
2. Greenwald, T.; Bennartz, R.; O'Dell, C.; Heidinger, A. Fast computation of microwave radiances for data assimilation using the “Successive Order of Scattering” method. *J. Appl. Meteorol.* **2005**, *44*, 960–966.
3. Cavalieri, D.J.; Parkinson, C.L.; DiGirolamo, N.; Ivanoff, A. Intersensor calibration between F13 SSMI and F17 SSMIS for global sea ice data records. *IEEE Geosci. Remote Sens. Lett.* **2012**, *9*, 233–236.
4. Kunkee, D.B.; Swadley, S.D.; Poe, G.A.; Hong, Y.; Werner, M.F. Special Sensor Microwave Imager Sounder (SSMIS) radiometric calibration anomalies. Part I: Identification and characterization. *IEEE Trans. Geosci. Remote Sens.* **2008**, *46*, 1017–1033.
5. Cao, C.; Weinreb, M.; Xu, H. Predicting simultaneous Nadir overpasses among polar-orbiting meteorological satellites for the intersatellite calibration of radiometers. *J. Atmos. Ocean. Technol.* **2004**, *21*, 537–542.
6. Wilheit, T.T. Comparing calibrations of similar conically scanning window-channel microwave radiometers. *IEEE Trans. Geosci. Remote Sens.* **2013**, *51*, 1453–1464.
7. Yan, B.; Weng, F. Intercalibration between special sensor microwave imager/sounder and special sensor microwave imager. *IEEE Trans. Geosci. Remote Sens.* **2008**, *46*, 984–995.

8. Wentz, F.J.; Meissner, T. *Algorithm Theoretical Basis Document (ATBD)*; Version 2; RSS Tech. Proposal 121599A-1; Remote Sensing Systems: Santa Rosa, CA, USA, 2000.
9. Gentemann, C.L.; Wentz, F.J.; Brewer, M.; Hilburn, K.; Smith, D. Passive Microwave Remote Sensing of the Ocean: An Overview. In *Oceanography from Space*; Barale, V., Gower, J.F.R., Alberotanza, L., Eds.; Springer: The Hague, The Netherlands, 2010; pp. 13–33.
10. Liu, Q.; Weng, F.; English, S.J. An improved fast microwave water emissivity model. *IEEE Trans. Geosci. Remote Sens.* **2011**, *49*, 1238–1250.
11. Wentz, F.J. A well-calibrated ocean algorithm for special sensor microwave/imager. *J. Geophys. Res.* **1997**, *102*, 8703–8718.
12. Saunders, R.; Matricardi, M.; Brunel, P. An improved fast radiative transfer model for assimilation of satellite radiance observations. *Quart. J. Roy. Meteorol. Soc.* **1999**, *125*, 1407–1425.
13. Anguelova, M.D.; Gaiser, P.W. Dielectric and radiative properties of sea foam at microwave frequencies: Conceptual understanding of foam emissivity. *Remote Sens.* **2012**, *4*, 1162–1189.
14. Basharinov, A.E.; Kutuzova, B.G. Investigation of cloud atmosphere emission and absorption in millimeter and centimeter wave ranges. *VMGO Trans.* **1968**, *222*, 100–110.
15. Wentz, F.J.; Spencer, R.W. SSM/I rain retrievals within a unified all-weather ocean algorithm. *J. Atmos. Sci.* **1998**, *55*, 1613–1627.
16. Hilburn, K.A.; Wentz, F.J. Intercalibrated passive microwave rain products from the Unified Microwave Ocean Retrieval Algorithm (UMORA). *J. Appl. Meteorol. Climatol.* **2008**, *47*, 778–794.
17. Ulaby, F.T.; Moore, R.K.; Fung, A.K. *Microwave Remote Sensing Fundamentals and Radiometry*. In *Microwave Remote Sensing: Active and Passive*; Addison-Wesley Publishing Co.: Reading, MA, USA, 1981; Volume 1.
18. Turner, D.S. Systematic errors inherent in the current modeling of the reflected downward flux term used by remote sensing models. *Appl. Opt.* **2004**, *43*, 2369–2383.
19. Guldner, J. A model-based approach to adjust microwave observations for operational applications: Results of a campaign at Munich Airport in winter 2011. *Atmos. Meas. Tech.* **2013**, *6*, 2879–2891.
20. Aulign  T.; McNally, A.P.; Dee, D.P. Adaptive bias correction for satellite data in a numerical weather prediction system. *Quart. J. Roy. Meteorol. Soc.* **2007**, *133*, 631–642.
21. Bobylev, L.P.; Zabolotskikh, E.V.; Mitnik, L.M.; Mitnik, M.L. Atmospheric water vapor and cloud liquid water retrieval over the Arctic Ocean using satellite passive microwave sensing. *IEEE Trans. Geosci. Remote Sens.* **2010**, *48*, 283–294.
22. Zabolotskikh, E.V.; Mitnik, L.M.; Chapron, B. New approach for severe marine weather study using satellite passive microwave sensing. *Geophys. Res. Lett.* **2013**, *40*, 1–4.
23. Stogryn, A. The apparent temperature of the sea at microwave frequencies. *IEEE Trans. Antennas Propag.* **1967**, *15*, 278–286.
24. Hollinger, J.P. Passive microwave measurements of sea surface roughness. *IEEE Trans. Geosci. Electron.* **1971**, *9*, 165–169.
25. Tsang, L.; Kong, J.A.; Shin, R.T. Solutions of Radiative Transfer Equations with Applications to Remote Sensing. In *Theory of Microwave Remote Sensing*, 1st ed.; Wiley-Interscience: Hoboken, NJ, USA, 1985; pp. 214–235.

26. Stogryn, A. The emissivity of sea foam at microwave frequencies. *J. Geophys. Res.* **1972**, *77*, 1658–1666.
27. Smith, P.M. The emissivity of sea foam at 19 and 37 GHz. *IEEE Trans. Geosci. Remote Sens.* **1988**, *26*, 541–547.
28. Bortkovskii, R.S. *Air-Sea Exchange of Heat and Moisture during Storms*; Springer: New York, NY, USA, 1987.
29. Cox, C.; Munk, W. Measurement of the roughness of the sea surface from photographs of the sun's glitter. *J. Opt. Soc. Amer.* **1954**, *44*, doi:10.1364/JOSA.44.000838.
30. Mitsuyasu, H.; Honda, T. Wind-induced growth of water waves. *J. Fluid Mech.* **1982**, *123*, 425–442.
31. Monahan, E.C.; Muircheartaigh, I.Ó. Optimal power-law description of oceanic whitecap coverage dependence on wind speed. *J. Phys. Oceanogr.* **1980**, *10*, 2094–2099.
32. Guissard, A.; Sobieski, P. An approximate model for the microwave brightness temperature of the sea. *Int. J. Remote Sens.* **1987**, *8*, 1607–1627.
33. Meissner, T.; Wentz, F.J. The emissivity of the ocean surface between 6 and 90 GHz over a large range of wind speeds and earth incidence angles. *IEEE Trans. Geosci. Remote Sens.* **2012**, *50*, 3004–3026.
34. Padmanabhan, S.; Reising, S.C.; Asher, W.E.; Rose, L.A.; Gaiser, P.W.; Bobak, J.P.; Dowgiallo, D.J.; Anguelova, M. Azimuthal Dependence of the Microwave Emission from Foam Generated by Breaking Waves at 18.7 and 37 GHz. In Proceedings of 2006 IEEE MicroRad, SanJuan, Puerto Rico, 28 February–3 March 2006; pp. 131–136.
35. Yueh, S.H. Modeling of wind direction signals in polarimetric sea surface brightness temperatures. *IEEE Trans. Geosci. Remote Sens.* **1997**, *35*, 1400–1418.
36. Jones, W.L.; Black, P.G.; Boggs, D.M.; Bracalente, E.M.; Brown, R.A.; Dome, G.; Ernst, J.A.; Halberstam, I.M.; Overland, J.E.; Peteherych, S.; *et al.* Seasat scatterometer: Results of the Gulf of Alaska workshop. *Science* **1979**, *204*, 1413–1415.
37. Aziz, M.A.; Reising, S.C.; Asher, W.E.; Rose, L.A.; Gaiser, P.W.; Horgan, K.A. Effects of air-sea interaction parameters on ocean surface microwave emission at 10 and 37 GHz. *IEEE Trans. Geosci. Remote Sens.* **2005**, *43*, 1763–1774.
38. Webster, W.J., Jr.; Wilheit, T.T.; Ross, D.B.; Gloersen, P. Spectral characteristics of the microwave emission from a wind-driven foam-covered sea. *J. Geophys. Res.* **1976**, *81*, 3095–3099.
39. Rosenkranz, P.W. Rough-sea microwave emissivities measured with the SSM/I. *IEEE Trans. Geosci. Remote Sens.* **1992**, *30*, 1081–1085.
40. Meissner, T.; Wentz, F. Ocean Retrievals for WindSat: Radiative Transfer Model, Algorithm, Validation. In Proceedings of MTS/IEEE (OCEANS'05), Santa Rosa, CA, USA, 20–23 June 2005; pp. 130–133.
41. Shibata, A. A wind speed retrieval algorithm by combining 6 and 10 GHz data from advanced microwave scanning radiometer: Wind speed inside hurricanes. *J. Oceanogr.* **2006**, *62*, 351–359.
42. Uhlhorn, E.W.; Black, P.G.; Franklin, J.L.; Goodberlet, M.; Carswell, J.; Goldstein, A.S. Hurricane surface wind measurements from an operational stepped frequency microwave radiometer. *Month. Wea. Rev.* **2007**, *135*, 3070–3085.
43. Chapron, B.; Bingham, A.; Collard, F.; Donlon, C.; Johannessen, J.A.; Piolle, J.F.; Reul, N. Ocean Remote Sensing Data Integration-Examples and Outlook. In Proceedings of OceanObs'09:

Sustained Ocean Observations and Information for Society, Venice, Italy, 21–25 September 2009; ESA Publications Division: Frascati, Italy, 2010; Volume 1, ESA Publication WPP-306.

44. Klein, L.; Swift, C. An improved model for the dielectric constant of sea water at microwave frequencies. *IEEE Trans. Antennas Propag.* **1977**, *25*, 104–111.
45. Wang, J.R. A comparison of the MIR-estimated and model-calculated fresh water surface emissivities at 89, 150, and 220 GHz. *IEEE Trans. Geosci. Remote Sens.* **2002**, *40*, 1356–1365.
46. Stogryn, A.P.; Bull, H.T.; Rubayi, K.; Iravanchy, S. *The Microwave Permittivity of Sea and Fresh Water*; GenCorp Aerojet: Azusa, CA, USA, 1995.
47. Ellison, W.; Balana, A.; Delbos, G.; Lamkaouchi, K.; Eymard, L.; Guillou, C.; Prigent, C. New permittivity measurements of seawater. *Radio Sci.* **1998**, *33*, 639–648.
48. Guillou, C.; Ellison, W.; Eymard, L.; Lamkaouchi, K.; Prigent, C.; Delbos, G.; Balana, G.; Boukabara, S.A. Impact of new permittivity measurements on sea surface emissivity modeling in microwaves. *Radio Sci.* **1998**, *33*, 649–668.
49. Meissner, T.; Wentz, F.J. The complex dielectric constant of pure and sea water from microwave satellite observations. *IEEE Trans. Geosci. Remote Sens.* **2004**, *42*, 1836–1849.
50. Waters, J.W. Absorption and Emission by Atmospheric Gases. In *Astrophysics Radio Telescopes*; Academic Press: Waltham, MA, USA, 1976; Volume 12, Part B, pp. 142–176.
51. Meirolt-Mautner, I.; Prigent, C.; Defer, E.; Pardo, J.R.; Chaboureau, J.P.; Pinty, J.P.; Mech, M.; Crewell, S. Radiative transfer simulations using mesoscale cloud model outputs: Comparisons with passive microwave and infrared satellite observations for midlatitudes. *J. Atmos. Sci.* **2007**, *64*, 1550–1568.
52. Liebe, H.J. An updated model for millimeter wave propagation in moist air. *Radio Sci.* **1985**, *20*, 1069–1089.
53. Liebe, H.J.; Layton, D.H. *Millimeter-Wave Properties of the Atmosphere: Laboratory Studies and Propagation Modeling*; Nat. Tech. Inf. Services: Boulder, CO, USA, 1987.
54. Liebe, H.J.; Hufford, G.A.; Cotton, M.G. Propagation Modeling of Moist Air and Suspended Water/Ice Particles at Frequencies below 1000 GHz. AGARD Conference Proceedings 542, Atmospheric Propagation Effects through Natural and Man-Made Obscurants for Visible through MM-Wave Radiation, 3.1-3.10, 1993. Available online: <http://ftp.rta.nato.int/public/PubFullText/AGARD/CP/AGARD-CP-542/CP-542-03.pdf> (accessed on 11 March 2014).
55. Rosenkranz, P.W. Water vapor microwave continuum absorption: A comparison of measurements and models. *Radio Sci.* **1998**, *33*, 919–928.
56. Cruz Pol, S.L.; Ruf, C.S.; Keilm, S.J. Improved 20-to 32-GHz atmospheric absorption model. *Radio Sci.* **1998**, *33*, 1319–1333.
57. Turner, D.D.; Cadeddu, M.P.; Lohnert, U.; Crewell, S.; Vogelmann, A.M. Modifications to the water vapor continuum in the microwave suggested by ground-based 150-GHz observations. *IEEE Trans. Geosci. Remote Sens. Lett.* **2009**, *47*, 3326–3337.
58. Makarov, D.S.; Tretyakov, M.Y.; Rosenkranz, P.W. 60-GHz oxygen band: Precise experimental profiles and extended absorption modeling in a wide temperature range. *J. Quant. Spectrosc. Radiat. Transf.* **2011**, *112*, 1420–1428.

59. Rothman, L.S.; Gordon, I.E.; Barbe, A.; Benner, D.C.; Bernath, P.F.; Birk, M.; Boudon, V.; Brown, L.R.; Campargue, A.; Champion, J.-P.; *et al.* The HITRAN 2008 molecular spectroscopic database. *J. Quant. Spectrosc. Radiat. Transf.* **2009**, *110*, 533–572.
60. Liljegren, J.C.; Boukabara, S.A.; Cady-Pereira, K.; Clough, S.A. The effect of the half-width of the 22-GHz water vapor line on retrievals of temperature and water vapor profiles with a 12-channel microwave radiometer. *IEEE Trans. Geosci. Remote Sens.* **2005**, *43*, 1102–1108.
61. Marchand, R.; Ackerman, T.; Westwater, E.R.; Clough, S.A.; Cady-Pereira, K.; Liljegren, J.C. An assessment of microwave absorption models and retrievals of cloud liquid water using clear-sky data. *J. Geophys. Res.* **2003**, *108*, doi:10.1029/2003JD003843.
62. Melsheimer, C.; Verdes, C.; Buehler, S.A.; Emde, C.; Eriksson, P.; Feist, D.G.; Ichizawa, S.; John, V.O.; Kasai, Y.; Kopp, G.; *et al.* Intercomparison of general purpose clear sky atmospheric radiative transfer models for the millimeter/submillimeter spectral range. *Radio Sci.* **2005**, *40*, 1–28.
63. Hewison, T.J.; Cimini, D.; Martin, L.; Gaffard, C.; Nash, J. Validating clear air absorption models using ground-based microwave radiometers and vice-versa. *Meteorol. Z.* **2006**, *15*, 27–36.
64. Clough, S.A.; Shephard, M.W.; Mlawer, E.J.; Delamere, J.S.; Iacono, M.J.; Cady-Pereira, K.; Boukabara, S.; Brown, P.D. Atmospheric radiative transfer modeling: A summary of the AER codes. *J. Quant. Spectrosc. Radiat. Transf.* **2005**, *91*, 233–244.
65. Kawanishi, T.; Sezai, T.; Ito, Y.; Imaoka, K.; Takeshima, T.; Ishido, Y.; Shibata, A.; Miura, M.; Inahata, H.; Spencer, R.W. The Advanced Microwave Scanning Radiometer for the Earth Observing System (AMSR-E), NASDA's contribution to the EOS for global energy and water cycle studies. *IEEE Trans. Geosci. Remote Sens.* **2003**, *41*, 184–194.
66. NOAA Comprehensive Large Array—Data Stewardship System (CLASS). Available online: <http://www.class.ncdc.noaa.gov> (accessed on 11 March 2014).
67. Sun, N.; Weng, F. Evaluation of special sensor microwave imager/sounder (SSMIS) environmental data records. *IEEE Trans. Geosci. Remote Sens.* **2008**, *46*, 1006–1016.
68. University of Wyoming. Available online: <http://weather.uwyo.edu/upperair/sounding.html> (accessed on 11 March 2014).
69. NOAA National Oceanographic Data Center. Available online: [http://www.nodc.noaa.gov/OC5/WOD/pr\\_wod.html](http://www.nodc.noaa.gov/OC5/WOD/pr_wod.html) (accessed on 11 March 2014).
70. Tretyakov, M.Y.; Koshelev, M.A.; Dorovskikh, V.V.; Makarov, D.S.; Rosenkranz, P.W. 60-GHz oxygen band: Precise broadening and central frequencies of fine-structure lines, absolute absorption profile at atmospheric pressure, and revision of mixing coefficients. *J. Mol. Spectrosc.* **2005**, *231*, 1–14.
71. Surface Weather Analysis. Available online: [http://www.wetter3.de/Archiv/archiv\\_dwd.html](http://www.wetter3.de/Archiv/archiv_dwd.html) (accessed on 11 March 2014).
72. Hanafin, J.; Quilfen, Y.; Arduin, F.; Sienkiewicz, J.; Queffeuilou, P.; Obrebski, M.; Chapron, B.; Reul, N.; Collard, F.; Corman, D. Phenomenal sea states and swell from a North Atlantic Storm in February 2011: A comprehensive analysis. *Bull. Am. Meteorol. Soc.* **2012**, *93*, 1825–1832.